

Interactive comment on “The recent amplifying seasonal cycle of the Arctic sea ice extent related to the subsurface cooling in the Bering Sea” by Xiao-Yi Yang and Guihua Wang

Xiao-Yi Yang and Guihua Wang

xyyang@xmu.edu.cn

Received and published: 25 August 2019

This paper shows that the Bering Sea was a major contributor to the increased amplitude of the seasonal cycle of pan-Arctic ice extent in the first decade of the 21st century. Perhaps more importantly, The paper is seriously dated before it even gets into the publication process.

Reply: Thank you for reminding us of this important information! We follow your advice and update all of the available datasets to the latest: (1) NSIDC monthly sea ice concentration data from November 1978 to June 2019; (2) ECMWF ERA-interim meteorological fields data from January 1979 to April 2019; (3) ECMWF ORA-S4 ocean

C1

fields data from January 1958 to December 2017; (4) JISAO PDO index from January 1900 to September 2018; (5) NCEP GODAS ocean assimilation data from January 1980 to May 2019; (6) HadEN4.2.1 g10 ocean subsurface analyses data from January 1950 to December 2018. To probe into the physical mechanism related to the sea ice change, we download two other datasets, i.e., WHOI OAflux data from January 1958 to December 2018 and NPGO index constructed by Di Lorenzo from January 1950 to December 2018. All above changes are described in the revised paper Section 2.

Once total Arctic sea ice extent time series is extended to the latest, its variation magnitude seems drop down again. That is, 2013-2018 annual standard deviation is overall lower than that of 2007-2012, representing a flavor of decadal scale oscillation feature (Fig. 1a). Fig. 1b shows the standard deviation differences for each month. It is obvious that discrepancies between the three periods (2007-2012 minus 1979-2006, and 2013-2018 minus 2007-2012) are primarily come from the summer (Aug-Oct, peak in Sep) and spring (Mar-May, peak in April) seasons. The spatial patterns further show that the Pacific section including the Chukchi sea and the Bering Sea (gray fan) as well as the Laptev and eastern Siberian seas is the major contributor to these decadal changes of total Arctic sea ice extent. The normalized Chukchi-Bering SIE indices in ASO and MAM (fig. 2) both exhibit abrupt change since 2007. In summer this change can be viewed as a mean state mutation or regime shift (fig. 2a), while in spring it is more like a decadal oscillation (fig. 2b). In another words, the substantial retreat of Chukchi sea ice in summer and growth of Bering sea ice in spring occurs synchronously in 2007, collaborating on the soaring up of the totalArcSIE std. The dropping down of annual std since 2013, however, should be primarily attributed to the spring Bering sea ice decline.

We made these revisions in the section 3.1 of the revised manuscript.

Fig. 1 (a) time series of monthly total Arctic sea ice extent (totalArcSIE) anomalies (climatology calculated during 1979-1998, upper panel) and annual standard deviation (lower panel) during the period of 1978-2019. Red lines denote the mean values for

C2

different periods. Vertical blue line indicates the critical year of 2007. (b) monthly differences of standard deviation for three periods designated in (a) lower panel. Black line denotes the values of 2007-2012 minus 1979-2006. Red line denotes the values of 2013-2018 minus 2007-2012. Blue dashed lines are the two peak months, September (thick) and April (thin). (c) Sum of August-October mean sea ice concentration (SIC) standard deviation differences between the three periods (absolute values of 0712-7906 (black lines in fig. 1b) plus absolute values of 1318-0712 (red lines in fig.1 b)). Solid contours mark the climatological sea ice edges (SIC=15%) for three periods. The Chukchi-Bering sector is delimited by the gray fan-shaped frame. (d) Same as (c), but for March-May mean.

Fig. 2 (a) Normalized summer (August-October mean) ChukBerSIE index. (b) Normalized spring (March-May mean) ChukBerSIE index (SBII, black bars), superposed by its decadal component (blue lines). Red dashed lines mark the threshold of ± 0.7 standard deviation for selecting the composite years. Vertical blue line indicates the critical year of 2007.

(2) The explanation for the Bering Sea ice history, especially its decadal-scale variability, leaves the reader wondering about the value added..... In short, the paper does not provide a compelling explanation for the Bering Sea winter/spring ice expansion of 2008-2013 (let alone the spectacular abrupt decrease in 2018 and 2019).

Reply: Thank you for your suggestions! As we noted in the original manuscript, the spring Bering sea ice high index is associated a SLP dipole pattern prior-2007 but an anomalous high pressure thereafter (figure not shown here). Furthermore, the anomalous Bering SST anomalies exhibits a close connection with North Pacific large-scale SST pattern in the recent decade, in great contrast to the isolated Bering SST variability before 2007 (fig. 3a & b). In addition, the SST anomalies can extend down to subsurface layer after 2007 (fig. 3c & d). This remarkable pattern change, together with the period extension of SBII variation from interannual to decadal scale (fig. 2b), suggests that the spring Bering sea ice variability is getting predominant by the ocean dynamical

C3

processes in Pacific. Numerous previous studies asserted that extra-tropical North Pacific climate variability is dominated by two decadal-scale ocean-atmosphere coupled modes, the Pacific Decadal Oscillation (PDO) (Mantua et al. 1997) and the North Pacific Gyre Oscillation (NPGO) (Di Lorenzo et al. 2008). Though defined independently as the first and second basin-scale EOF modes of sea surface temperature anomalies as well as sea surface height anomalies in the north Pacific Ocean respectively, the PDO and NPGO bear strong resemblance in their physical mechanisms and climate effect. They both are forced by the El Nino-like tropical Pacific SSTA (Newman et al. 2003; Di Lorenzo et al. 2010), feedback to the western Pacific Kuroshio-Oyashio extension through the ocean Rossby wave propagation (Schneider and Cornuelle 2005; Ceballos et al. 2009), and impact the low-frequency variability of marine ecosystem system (Miller et al. 2004; Di Lorenzo et al. 2013; Sydeman et al. 2013). Besides the remote tropical ENSO forcing, the PDO and NPGO can be driven by the local ocean-atmosphere interaction. The ocean, as a low-frequency filter, integrates the atmospheric stochastic noise and trigger the decadal-scale oscillation (Newman et al. 2016; Yi et al. 2015). The corresponding large-scale atmospheric modes are the Aleutian Low variability (for PDO) and the North Pacific Oscillation (for NPGO).

In the light of previous study fruits, we infer that the SSTA pattern shown in fig. 3b may relate to the pacific decadal variability. Fig. 4 shows the spring PDO and NPGO patterns for the two periods. The PDO positive phase is associated with the deepening of Aleutian Low, warming in the northeast of Pacific including the Gulf of Alaska and the California coast, paralleling cooling in the Kuroshio extension. Moderate warming in the eastern equatorial Pacific is discernable (Fig 4a). In the recent decade, however, the PDO SLP anomalies abate but the eastern Pacific warming enhances greatly. Notably the Bering Sea and the central equatorial Pacific stand out to be among the most significant warming regions (Fig 4c). The spring positive NPGO corresponds to an anomalous high pressure over the most of North Pacific and negative SLP anomalies over the eastern Asian and Alaska in the early period. The SSTA spatial pattern looks like the PDO SSTA pattern shown in fig 4a but with a quarter phase difference (fig.

C4

4b), which is an allusion of orthogonality between these two modes. The change of NPGO pattern after 2007 is conspicuous: The quadruple SLP anomalies coupling the significant cooling extending all the way from the Bering Sea, the northeastern Pacific to the central Pacific (fig. 4d). It seems that both the PDO and NPGO contribute to the Bering SST anomalies in this decade.

To reaffirm the impact of PDO and NPGO onto the Bering Sea temperature, the running regression is computed from Jan1950 to dec2018 as shown in fig. 5a & b. The Bering temperature indeed exhibits close connection with PDO since the mid-1970s. The correlation first appears in the subsurface layer, then enhances and extends upward with the time evolution, reaching its peak near the surface after 2000. The impact of NPGO, however, is significant only in the 1970s-1980s and after 2005. Fig. 5c shows the 241-month running correlation between the PDO and NPGO indices. There is almost zero correlation before 1990s and significant negative correlation in the new century. By scrutinizing the annual mean PDO and NPGO time series (fig. 6), one can easily perceive increasing synchronism of decadal-scale phase change in recent years. The PDO period is obviously shortened from the traditional 20-40 years to around 10-15 years after 1990s. The NPGO, on the other hand, maintains its periodicity stable, but the oscillation magnitude is almost doubled from the end of 1980s. The strengthening of NPGO and the PDO coalesce to form the apparent anti-resonance after 2007. The synchronization of PDO and NPGO and their common effects on the Bering Sea temperature since 2007 may account for the recent decadal oscillation of spring Bering Sea ice extent.

The robust cause and effect should be based on the establishment of physical linkage. We thereafter explore how the PDO and NPGO modes collaborate to the significant Bering sea temperature anomalies in the recent decade. In spite of high resemblance of SSTA patterns (fig. 4 c & d), great contrast of their SLP patterns between these two modes suggests different atmospheric forcing and consequently distinct oceanic physical processes. Firstly, the surface turbulent heat flux anomalies are regressed on

C5

PDO and NPGO indices (fig. 7). There is hardly significant heat flux anomaly in the Bering area with positive one standard deviation of PDO for the whole period (fig. 7 a & c). The positive phase of NPGO corresponds to the reduced upward heat flux along the northwestern coast of Bering in the early period (fig. 7b). In the later period, the positive and negative anomalies of heat flux appear in the southern and northern Bering Sea respectively, with the zero line approximately along the climatological spring Bering sea ice edge (fig. 7d). Referring to the quadruple SLP pattern (fig. 4d), the anomalous atmospheric cold advection prevails over the Bering Sea, leading to the drop-down of atmospheric surface temperature, then increased heat loss over the open ocean and the negative anomalies of SST. The sea ice expansion follows the decreasing temperature and insulates the ocean-atmosphere exchange, resulting in the negative anomalies of heat flux over the ice cover. This thermodynamic process emerges in the later period, primarily owing to the atmospheric SLP quadruple pattern.

Besides the thermodynamic effect, the NPGO SLP pattern change may play a role in dynamical adjustment of the Bering Sea through its effect on wind stress and Ekman pumping rate. Therefore, the spring wind stress and Ekman pumping rate anomalies are regressed on PDO and NPGO indices respectively (fig. 8). In response to the deepening of AL (fig. 4 left panels), positive phase of PDO is associated with an anomalous cyclonic circulation over the north Pacific without notable decadal change. The relevant positive Ekman pumping anomalies mainly reside in the north Pacific open ocean, while the enhanced northeasterly prevails over the entire Bering Sea (fig. 8a & c). In contrast, the NPGO can hardly cast a spell on the large-scale circulation. Nevertheless, the scattered significant wind stress anomalies in the later period organize an anomalous anti-cyclonic pattern, hence the negative Ekman pumping rate (downwelling) in the western Bering Sea (fig. 8d). The vertical velocity induced by surface wind stress curl usually results in the displacement of thermocline or pycnocline, followed by the dynamical adjustment of the subsurface ocean.

The oceanic density and zonal and meridional velocity anomalies are regressed on the

C6

PDO index (fig. 9). The large-scale cyclonic wind stress anomalies associated with the PDO positive phase (fig. 8 left panels) lead to the strengthening of Alaska stream and enhanced northward transport of heat along the Bering slope, contributing to the surface warming and density decrease in the Bering Sea (fig. 9a). In the subsurface layer, however, the wind-driven component abates rapidly with depth. The anomalous heat transport is limited to the boundary current around the southern Bering deep basin (fig. 9b). Therefore, the Bering Sea warming associated with PDO peaks in the mixed layer (fig. 5a). The circulation anomalies corresponding to NPGO is also investigated, but without any remarkable signal of current and heat transport anomalies (figure not shown).

As the NPGO leads to the anomalous Ekman pumping (fig. 8d) and subsurface cooling (fig. 5b), we examine the pycnocline displacement and vertical exchange between the mixed layer and subsurface ocean in the Bering deep basin (160-190E, 50-60N). The climatological vertical profile of Bering basin (BB) mean temperature (T), salinity (S) and density (Rho) in spring is presented in fig. 10. The BB vertical stratification depends on salinity, with the highly matching of the position of pycnocline and halocline at about 100~300m depth. In striking contrast to the increase of salinity and density with depth, the temperature profile exhibits a sandwich-like pattern. There is a sharp rising of temperature from $\sim 2.5^{\circ}\text{C}$ to $\sim 3.5^{\circ}\text{C}$ in 100-300m, then slowly drop down with depth below the permanent pycnocline. It is clear that the cold and fresh water in the mixed layer is superposed over the warm and saline water in the pycnocline. The spring BB T/S/Rho anomalies associated with positive NPGO for different periods are shown in fig. 11. In the early period, NPGO-related changes of water property are confined in the mixed layer. In the later period, the T/S/Rho anomalies associated with positive one standard deviation of NPGO almost doubled in the mixed layer, and the change in the pycnocline can be detected clearly. The colder and saltier water in the surface overlies the less cold and fresher water in the subsurface, corresponding to the density increase (decrease) in the mixed layer (pycnocline).

C7

A NPGO-related atmosphere-ocean-ice feedback mechanism may be inferred as following: The quadruple SLP pattern in the recent decade (fig. 4d) favors the atmospheric cold advection and anticyclonic wind stress curl (fig. 8d) over the Bering Sea in association with the positive phase of NPGO. In response to atmospheric thermal forcing, ocean heat loss enhances in the open water (fig. 7d), leading to the greater surface cooling. On the other hand, the Bering sea ice cover expands with the cooling condition. Ice expansion is usually followed by surface salinification in the adjacent open water owing to brine-rejection effect. Surface water is getting denser with cooling and salinification anomalies. Triggered by the anticyclonic wind stress curl over the BB region, anomalous downwelling acts to push the subsurface isopycnals downward, hence the decrease of density and freshening in the pycnocline with the positive NPGO (fig. 11b). The reverse processes may occur for the negative NPGO phase: atmospheric warm advection leads to less heat loss from ocean and retreat of sea ice cover, thus warming and freshening of surface water. The surface density decreases to a large extent. The cyclonic wind stress forcing and the subsequent upwelling induce the heaving of subsurface isopycnals, hence increased density and salinification in the pycnocline. Once the pycnocline water property changes, it gets less exposure to surface flux damping and tends to persist for more than one year. This may at least partly account for the dramatic decadal oscillation of Bering SST and sea ice extent anomalies after the year of 2007.

To further verify the sensitivity of SBII to the NPGO-oriented physical processes, the spring wind stress and Ekman pumping rate anomalies are composited based on the SBII high minus low index years as shown in fig. 12. The spring Bering sea ice cover expansion corresponds to the prevailing northerly over the Bering Sea and a large-scale anticyclonic circulation and upwelling in the North Pacific Ocean in the early period, which resembles the PDO-related pattern (fig. 8a). For the later period, there are anomalous anticyclonic wind stress curl over the Bering Sea and downwelling in association with the increased ice extent, which resembles the NPGO-related pattern (fig. 8d). In addition, the Bering Basin water property changes in association with the

C8

SBII high minus low index years are also presented in fig. 13. In the early period, the ice expansion corresponds to the surface cooling but little change in the salinity and density. In the later period, the ice expansion corresponds to much larger magnitude of surface cooling as well as salinity and density anomalies. The change can also extend to pycnocline layer with the reverse of salinity and density anomalies vertically, which almost reproduces the NPGO-related T/S/Rho anomalies in fig. 11b.

In conclusion, it is the NPGO change and its synchronization with the PDO that trigger the recent decadal oscillation of Bering sea ice extent. This notable decadal oscillation in the Bering sea plays an important role to interpret recent total Arctic sea ice extent change. In the background of global warming and polar amplification, the total Arctic ice volume and thickness decrease persistently. It is conceivable that the future change of Arctic sea ice extent is more sensitive to the complicated air-sea coupling processes. Therefore, to better understand and predict the future Arctic sea ice change, we should pay more attention to these large-scale coupled modes such as Pacific decadal variability and Atlantic multi-decadal oscillation.

Fig. 3 Composites of (a)&(b) sea surface temperature anomalies; (c)&(d) subsurface (165m) water temperature anomalies based on the SBII high minus low index during the prior-2007 period (left panels) and the post-2007 period (right panels). Gray rectangle defines the area of Bering Sea (170-200E, 55-65N). Solid (dashed) lines enclose the positive (negative) values that are significant at the 95% confidence level.

Fig. 4 (a) Regression of March-May mean sea surface temperature anomalies (color shading) and sea level pressure anomalies (contour) on the PDO index during the period of 1979-2006. The contour interval is 0.2hPa. (b) Same as (a), but regression on the NPGO index. (c) & (d), same as (a) & (b), but during the period of 2007-2018.

Fig. 5 241 months running regression of the HadEN4.2.1 g10 Bering sea temperature anomalies on the PDO index (a) and on the NPGO index (b). All the data are preprocessed by 13 months low-pass filter. Solid (dashed) lines enclose the positive

C9

(negative) regression coefficients that are significant at the 95% confidence level. (c) 241 months running correlation between the PDO and NPGO indices. Black and red lines indicate the original monthly correlation and 13 months low-pass filtered correlation respectively.

Fig. 6 (a) Time series of the annual mean PDO index (black bar) superposed by its decadal component (blue line) during the period of 1950-2018. The red dashed lines indicate the critical year of 2007. (b) Same as (a), but the NPGO index.

Fig. 7 (a) & (b) Regression of March-May mean surface turbulent (sensible + latent) heat flux onto the PDO (left panels) and NPGO (right panels) indices during the period of 1979-2006. (c) & (d) Same as (a) & (b), but for the later period. Solid (dashed) lines enclose the positive (negative) regression coefficients that are significant at the 95% confidence level.

Fig. 8 Same as Fig. 7, but for the regression of surface wind stress (vector) and Ekman pumping rate (color shading) anomalies. Solid (dashed) lines enclose the positive (negative) regression coefficients of Ekman pumping that are significant at the 95% confidence level. The black (gray) vectors indicate the wind stress regression coefficients are significant (insignificant) at the 95% confidence level.

Fig. 9 (a) Regressions of surface (5m) density (color shading) and zonal and meridional velocities (vector) onto the PDO index. Solid (dashed) lines enclose the positive (negative) density anomalies that are significant at the 95% confidence level. Only the velocity anomalies that are significant at the 95% confidence level are plotted. (b) Same as (a), but for the subsurface layer (165m).

Fig. 10 Climatological vertical profile of spring (March-May) Bering deep basin (160-190E, 50-60N) mean temperature and salinity (a) and density (b).

Fig. 11 Regression of spring (March-May mean) Bering deep basin temperature, salinity and density on the NPGO index during the 1979-2006 period (a) and the 2007-2017

C10

period (b) for each depth layer. The marks of black dot, red cross and blue circle denote the regression coefficients that are significant at the 85% significant t test for density, temperature and salinity respectively.

Fig. 12 Composites of spring wind stress (vector) and Ekman pumping rate (color shading) based on the SBII high minus low index during the period of 1979-2006 (a) and the period of 2007-2018 (b).

Fig. 13 Same as fig. 11, but the composites based on SBII high minus low index.

Some specific comments:

1. Page 1, line 19: The decrease of pan-Arctic ice extent in recent decades has not really been “continuous”, as there have been ups and downs associated with interannual variability. One can also question the statement in line 20 that the “rate of ice loss accelerates from the 1990s”. If one calculates the trend of pan-Arctic September ice extent for the 2007-2018 period, the trend is essentially zero.

Reply: Some expressions are indeed not precise. We corrected them in the new manuscript. Thank you for pointing out this! The revision made in Page 1, line 24: Arctic sea ice has experienced a decline tendency and line 25: It is noteworthy that the remarkable ice retreat from the late 1990s.

2. Page 1, line 32: Not a sentence.

Reply: revised.

3. Page 4, line 32-33: In another example of the dated nature of the study, the PDO has been positive for nearly the entire period since 2015.

Reply: Thank you for reminding us about this! We extend our analysis period and reveal close linkage between the phase change of PDO and NPGO and the decadal oscillation of Bering Sea ice. Details please see the reply to your main point 2.

4. Page 6, lines 1-4: Figure 7 needs some elaboration, including an explanation of how

C11

Ekman pumping contributes to the proposed linkage between the atmosphere and the Bering Sea water temperatures and sea ice. In particular, what happens dynamically when Ekman pumping changes from negative to positive? What causes the sign reversal, and how do upwelling and downwelling relate to changes in water temperature? In other words, please present more information on the mechanistic linkage alluded to here.

Reply: We agree with your viewpoint and explore the detailed oceanic physical response to the atmospheric forcing in the revised manuscript. Details please see the reply to your main points.

5. Page 6, lines 22-31: There should be some description of the NPO and NPO-NPGO, and some supporting references. As it now stands, the NPO and NPGO seem to appear out of the blue.

Reply: Thank you so much for providing these clues! According to your suggestions, we compared the roles played by the PDO and NPGO in the Bering sea ice decadal changes and relevant physical processes. The conclusion is made that the NPGO changes and its synchronization with PDO mode may trigger the decadal change of Bering Sea. Details please see the reply to your main points.

Interactive comment on The Cryosphere Discuss., <https://doi.org/10.5194/tc-2019-37>, 2019.

C12

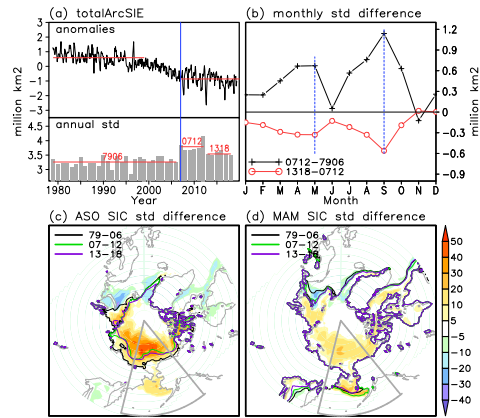


Fig. 1. Decadal change of total Arctic sea ice extent and its standard deviation

C13

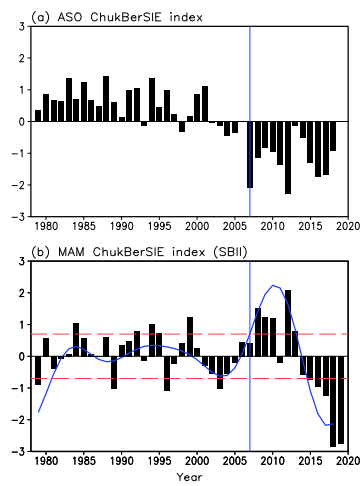


Fig. 2. Normalized ChukberSIE index in summer and spring

C14

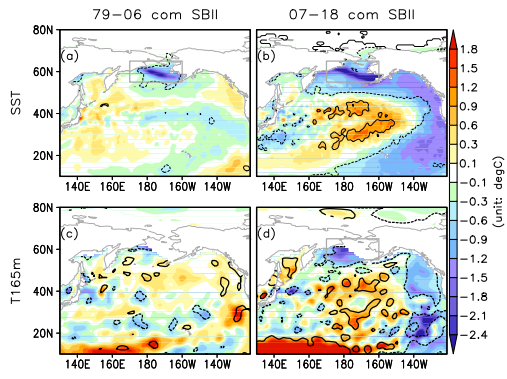


Fig. 3. Composites of SST and 165m T based on SBII index for the two periods

C15

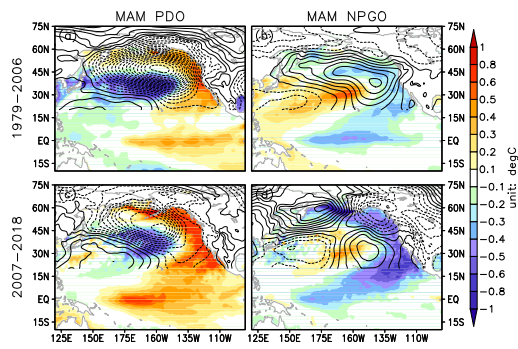


Fig. 4. Regressions of SST and SLP on the PDO and NPGO index for the two periods

C16

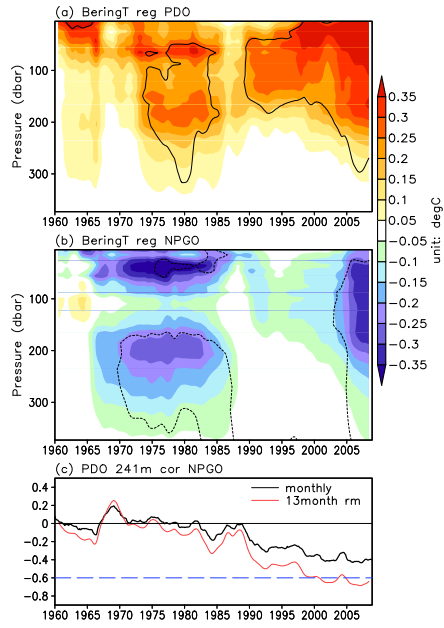


Fig. 5. Running regression of Bering sea temperature on the PDO and NPGOindex and running correlation between the two indices

C17

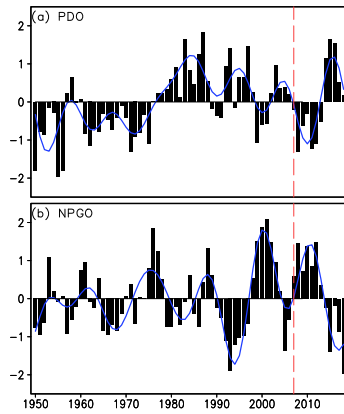


Fig. 6. Annual mean PDO and NPGO indices

C18

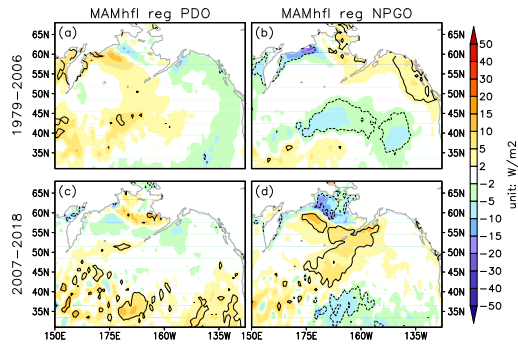


Fig. 7. Regression of surface turbulent heat flux onto the PDO and NPGO indices for the two periods

C19

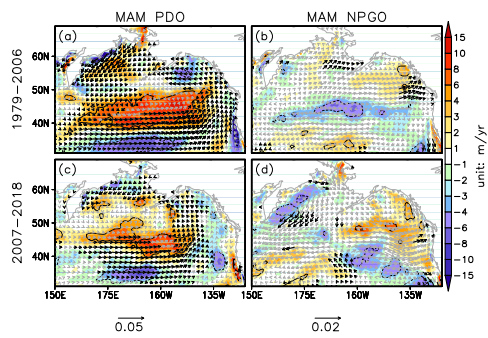


Fig. 8. Regressions of surface wind stress and Ekman puming rate onto the PDO and NPGO for the two periods

C20

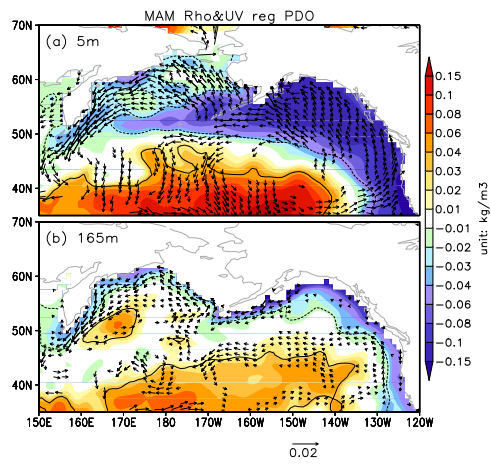


Fig. 9. Regressions of surface and subsurface density and zonal and meridional velocities onto the PDO

C21

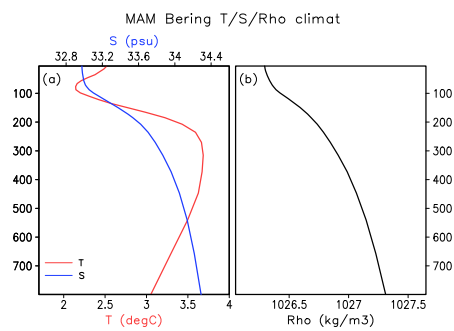


Fig. 10. Climatological vertical profile of spring Bering basin mean water properties

C22

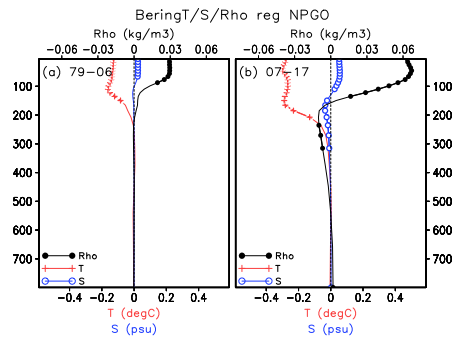


Fig. 11. Regression of spring Bering basin temperature, salinity and density onto the NPGO for the two periods

C23

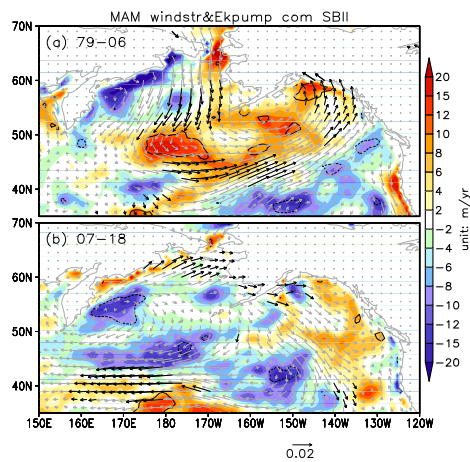


Fig. 12. Composites of spring wind stress and Ekman pumping rate based on the SBII index

C24

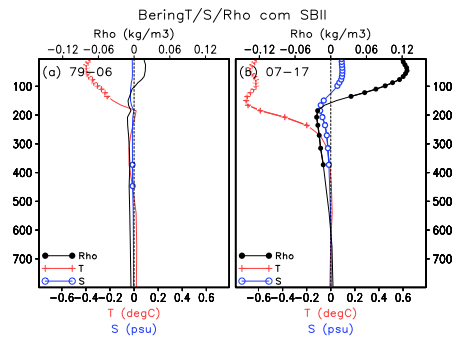


Fig. 13. Composites of Bering basin temperature, salinity and density based on the SBII index for the two periods